Strain-induced Megahertz Oscillation and Stable Velocity of an Antiferromagnetic Domain Wall

Fa Chen,[1,*] Xu Ge,[1,*] Wei Luo,[1,2,†] Renhao Xing,[1] Shiheng Liang,[3] Xiaofei Yang,[1] Long You,[1] Rui Xiong,[4] Yoshichika Otani,[5,6,7] and Yue Zhang[1,‡]

[1] *School of Optical and Electronic Information, Huazhong University of Science and Technology, Wuhan, China*
[2] *Wuhan National Laboratory for Optoelectronics, Huazhong University of Science and Technology, Wuhan, 430074, China*
[3] *Department of Physics, Hubei University, Wuhan, China*
[4] *Key Laboratory of Artificial Micro- and Nano-structures of Ministry of Education, School of Physics and Technology, Wuhan University, Wuhan, 430072, China*
[5] *Institute for Solid State Physics, University of Tokyo, Kashiwa 277-8581, Japan*
[6] *Quantum Nano-Scale Magnetism Team, CEMS-RIKEN, 2-1 Hirosawa, Wako 351-0198, Japan*
[7] *Trans-scale Quantum Science Institute, University of Tokyo, Bunkyo-ku, Tokyo 113-0033, Japan*

(Received 10 August 2020; revised 20 November 2020; accepted 11 December 2020; published 19 January 2021; corrected 12 October 2022)

Manipulation of magnetic domain walls (DWs) in an antiferromagnet plays a fundamental role in developing antiferromagnetic (AFM) devices with small size and high velocity for information processing. On the other hand, in addition to the ultrahigh-frequency (THz) AFM magnetization precession, recent investigation shows that an antiferromagnet may also exhibit unique dynamical behaviors at a lower frequency (GHz) by an optical method. In this work, we predict the characteristic frequency of AFM magnetization dynamics can be further widened to MHz by triggering the oscillation of an AFM DW under a stress that is a sinusoidal function in a spatial coordinate. This low frequency is due to the mismatch of size between the spatial period of stress and DW width. Based on this low-frequency oscillation, DW can move at an almost constant velocity by shifting the phase of stress. The proposition in this work paves the way to develop AFM devices with small size and ultralow dissipation.

DOI: 10.1103/PhysRevApplied.15.014030

I. INTRODUCTION

Due to the negligible stray field and magnetization precession at an ultrahigh frequency (THz), antiferromagnetic (AFM) spintronics attracts the attention of researchers aiming to develop devices with small volume and high speed for information processing or signal transmission [1,2]. In general, a femtosecond laser or spatiotemporal stress may trigger an ultrahigh-frequency (THz or near THz) magnetization precession due to the strong AFM exchange coupling [3–5]. Very recently, laser-induced unique AFM magnetization dynamics at a lower frequency (GHz) also attracts interest [6]. This widens the range of frequency for AFM devices.

The dynamics of magnetization is relevant to the structure of magnetization in an AFM medium. Usually, the magnetization structure in a real AFM medium is not as simple as a single domain. More complicated textures like skyrmions and multidomains with domain walls (DWs) may exist in the AFM material [7–17]. The manipulation of AFM textures plays a vital role in information processing or signal transmission in spintronic devices. The motion of AFM DWs or skyrmions is driven through the interaction with spin-polarized electrical currents, spin currents [7–9,12,13,18], temperature gradient [10], voltage [11,17], and spin wave [15]. In theory, an AFM DW moves at high velocity under an electrical current injecting into an AFM conductor or a heavy-metal layer above or below an AFM insulator [8,12,13]. Nevertheless, high dissipation from the electrical current is a bottleneck to application. On the other hand, in a single AFM insulator such as NiO, charge transportation is forbidden, and only other interactions with voltage or spin wave can drive a DW [11,15,17]. However, it is still challenging to trigger an AFM DW to move at a stable velocity under the applied voltage or spin wave. In voltage-induced AFM DW motion, an antiferromagnet is deposited on a wedge-shaped piezoelectric substrate, and a DW keeps accelerating due to sloped magnetic

[*] These authors contributed equally.
[†] Corresponding author. hustluowei@gmail.com
[‡] Corresponding author. yue-zhang@hust.edu.cn

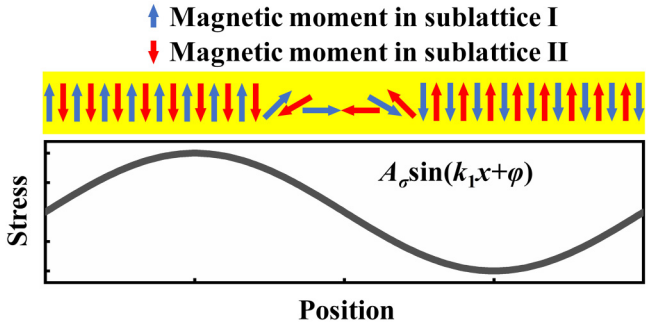

FIG. 1. Schematic of a Néel-type DW in an AFM nanowire under stress as a sinusoidal function in a spatial coordinate. (The spatial period of stress is much longer than DW width.)

anisotropy energy [11,17]. As for spin-wave-induced DW motion, DW velocity significantly enhances when the frequency of spin wave matches the characteristic frequency of an AFM DW [15]. Nevertheless, this is an *instantaneous* velocity at an equilibrium position but not a stable one.

In this work, we predict low-frequency (MHz) oscillation and nearly uniform motion of an AFM DW under stress as a sinusoidal function in a spatial coordinate. The size mismatch between the spatial period of stress and the DW width contributes to the low frequency of the DW oscillation. Since near-THz oscillation of magnetization in a single domain under a voltage-induced stress has been predicted [5], our work reveals possible voltage-induced magnetization dynamics with frequency ranging from MHz to near THz in a multidomain AFM system.

II. MODEL AND METHOD

We consider DW motion in an AFM nanowire under stress as a sinusoidal function in a spatial coordinate (Fig. 1). A DW is initially generated in the middle of the wire, and it exhibits Néel-type structure owing to the shape anisotropy of the one-dimensional (1D) chain (see Fig. S1 within the Supplemental Material for more details [19]). In general, position-dependent stress leads to a spatially varied magnetic anisotropy energy that triggers a DW to move in the direction with reducing anisotropy energy [17]. Under stress as a sinusoidal function in a spatial coordinate, the AFM DW may oscillate around the equilibrium position because of DW inertia [1,17]. The DW oscillation is relevant to the size difference between the spatial period of stress and DW width. Based on widely used technology for device fabrication like UV lithography, the allowed minimum spatial period of stress is at least hundreds of nanometers, which is significantly larger than DW width (several nanometers).

Quantitatively, the oscillation of an AFM DW is analyzed using the collective coordinate method (CCM). The calculation is based on a quasi-1D model, which assumes an AFM exchange coupling along the length direction (x axis) of a nanowire but neglecting the AFM coupling in the other two dimensions (y and z axes) [17]. The AFM nanowire comprises two sublattices (I and II), and the magnetization of each lattice I (II) is $\vec{m}_{\mathrm{I(II)}}(\vec{r},t)$. In an AFM system, the uniform magnetization $\vec{m}(\vec{r},t)$ and staggered order parameters $\vec{n}(\vec{r},t)$ are, respectively, expressed as $\vec{m}(\vec{r},t) = \vec{m}_{\mathrm{I}}(\vec{r},t) + \vec{m}_{\mathrm{II}}(\vec{r},t)$ and $\vec{n}(\vec{r},t) = [\vec{m}_{\mathrm{I}}(\vec{r},t) - \vec{m}_{\mathrm{II}}(\vec{r},t)]/l(\vec{r},t)$. Here $l(\vec{r},t)$ is the absolute value of $\vec{m}_{\mathrm{I}}(\vec{r},t) - \vec{m}_{\mathrm{II}}(\vec{r},t)$ and close to $2M_S$ for strong AFM exchange coupling. Here M_S is the saturation magnetization of the sublattice.

Under continuous approximation, the free energy of the quasi-1D AFM model is [15]

$$H \approx \int_v \left[\frac{J}{2}(\vec{m})^2 + \frac{A}{2}\left(\frac{d\vec{n}}{dx}\right)^2 - Kn_z^2\right] d\tau. \tag{1}$$

In Eq. (1), J is a homogeneous exchange energy constant, and $J \approx A/(ld)^2$. Here d is the lattice constant [15]. A is an exchange stiffness constant, and K is an anisotropy constant, including an intrinsic anisotropy constant (K_0) of an AFM insulator and position-dependent K_σ induced by stress, which we explain later in more detail. $d\tau$ is the volume element.

Based on Eq. (1), the effect fields of $\vec{m}$ and $\vec{n}$ are derived as $\vec{H}_m = -(\delta H/\mu_0 \delta \vec{m}) = -(J\vec{m}/\mu_0)$ and $\vec{H}_n = -(\delta H/\mu_0 \delta \vec{n}) = (1/\mu_0)[A(d^2\vec{n}/dx^2) + 2Kn_z\vec{e}_z]$. Here μ_0 is the permeability of vacuum. Starting from the Landau-Lifshitz-Gilbert (LLG) equation for the magnetization dynamics in the sublattice, we formulate the dynamics equations for $\vec{m}$ and $\vec{n}$ under the approximation of strong exchange coupling [14,15,17]:

$$\partial_t \vec{m} = -\gamma \vec{n} \times \vec{H}_n + 2\alpha M_S \vec{n} \times \partial_t \vec{n}, \tag{2}$$

$$\partial_t \vec{n} = -\gamma \vec{n} \times \vec{H}_m + \frac{\alpha}{2M_S} \vec{n} \times \partial_t \vec{m}. \tag{3}$$

In Eqs. (2) and (3), γ and α are the gyromagnetic ratio of an electron and damping parameter, respectively. Combining Eqs. (2) and (3) under linear approximation, we derive the dynamics equation of $\vec{n}$ [20]:

$$\frac{\partial^2 \vec{n}}{\partial t^2} + \frac{2J\alpha\gamma M_S}{\mu_0}\frac{\partial \vec{n}}{\partial t} = \frac{J\gamma^2}{\mu_0}\vec{H}_n. \tag{4}$$

In general, $\vec{n} = \vec{n}\{x, [q_1(t), q_2(t)]\}$ with q_1 and q_2 representing two collective coordinates of a magnetic texture. Multiplying both sides of Eq. (4) by $\partial\vec{n}/\partial q_1$ and $\partial\vec{n}/\partial q_2$ and integrating them over the space of nanowire, one can derive the following equation [20]:

$$\overleftrightarrow{M} \cdot \frac{d^2\vec{q}}{dt^2} + \frac{2J\alpha\gamma M_s}{\mu_0}\overleftrightarrow{M} \cdot \frac{d\vec{q}}{dt} = \vec{F}. \tag{5}$$

Here, $\overleftrightarrow{M}$ is the tensor of effective mass with its component $M_{ij} = \int_{-\infty}^{+\infty} (\partial\vec{n}/\partial q_i)\cdot(\partial\vec{n}/\partial q_j)dx$, and $F_i = (J\gamma^2/\mu_0)\int_{-\infty}^{+\infty} \vec{H}_n \cdot (\partial\vec{n}/\partial q_i)dx$.

We discuss the stress-driven DW motion. In the above equations $\vec{H}_n$ solely originates from the stress-induced anisotropy energy density (F_σ) of a cubic magnetostrictive system [21,22]:

$$F_\sigma = -\frac{3}{2}\lambda_s(\alpha_1^2\sigma_{xx} + \alpha_2^2\sigma_{yy} + \alpha_3^2\sigma_{zz} + 2\alpha_1\alpha_2\sigma_{xy} + 2\alpha_2\alpha_3\sigma_{yz} + 2\alpha_3\alpha_1\sigma_{xz}). \quad (6)$$

Here λ_s and σ_{ij} $(i, j = x, y, z)$ are isotropic magnetostrictive coefficient and stress tensor, respectively. α_1, α_2, and α_3 are the direction cosines of a staggered vector. We only consider the σ_{xx} component that can be approximated as$\sigma_{xx} = A_\sigma \sin(k_1 x + \varphi)$ with amplitude A_σ and phase φ. The validity of this simplicity is discussed below.

Because of the geometry of the AFM wire and the intrinsic anisotropy field along the z axis, the magnetization rotation is assumed to be confined in the x-z plane. Therefore, Eq. (6) is simplified to $F_\sigma = -K_\sigma\alpha_3^2 = (3/2)\lambda_s A_\sigma \sin(k_1 x + \varphi)\alpha_3^2$. Correspondingly, $\vec{H}_n$ is

$$\vec{H}_n = -\frac{3}{\mu_0}\lambda_s A_\sigma \sin(k_1 x + \varphi) n_z \vec{e}_z. \quad (7)$$

In a Walker DW, $\vec{n} = (\sin\theta\cos\phi, \sin\theta\sin\phi, \cos\theta)$, and $q_1 = q$ (the central position of DW), and $q_2 = \phi$ (the azimuthal angle of the magnetic moment in the central of DW), and $\theta = 2\arctan\{\exp[(x-q)/\lambda\}$ with $\lambda = \sqrt{A/K}$ for DW width [15]. Since the spatial period of stress is much longer than the DW width, we can neglect the variation of λ with K, where λ is approximated as$\sqrt{A/K_0}$.

Finally, we derive the dynamics equations for q and ϕ:

$$\frac{d^2q}{dt^2} + \frac{2J\alpha\gamma M_s}{\mu_0}\frac{dq}{dt} = \frac{3J\lambda\gamma^2}{2\mu_0^2}\lambda_s A_\sigma \cos(k_1 q + \varphi) g(k_1\lambda), \quad (8)$$

$$\frac{d^2\phi}{dt^2} + \frac{2J\alpha\gamma M_s}{\mu_0}\frac{d\phi}{dt} = 0.$$

Here $g(k_1\lambda) = \int_{-\infty}^{+\infty} \sin(k_1\lambda\varepsilon)\mathrm{sech}^2(\varepsilon)\tanh(\varepsilon)\mathrm{d}\varepsilon$ with $\varepsilon = (x-q)/\lambda$. The $g(k_1\lambda)$ can be analytically expressed as $g_a(k_1\lambda) = \pi(k_1\lambda)^2/\{2\sinh[\pi(\mathrm{k}_1\lambda)/2]\}$. Since the dynamics equation for q is independent on ϕ, we focus on the evolution of q in the following.

The following discussion is based on numerically solving Eq. (8), and we see the factor $g(k_1\lambda)$ is vital to the low frequency of DW oscillation. At first, we consider the motion of an AFM DW under position-dependent stress that is a sinusoidal function of x with a fixed phase φ ($\varphi = 0$). Afterwards, the phase φ is shifted at different time to trigger DW motion with a nearly stable velocity.

At first, DW is assumed to move under position-dependent stress with a zero damping coefficient $\alpha = 0$. In this case, Eq. (8) is converted into

$$\frac{d^2\beta}{dt^2} + \tilde{g}k_1 \sin(\beta) = 0. \quad (9)$$

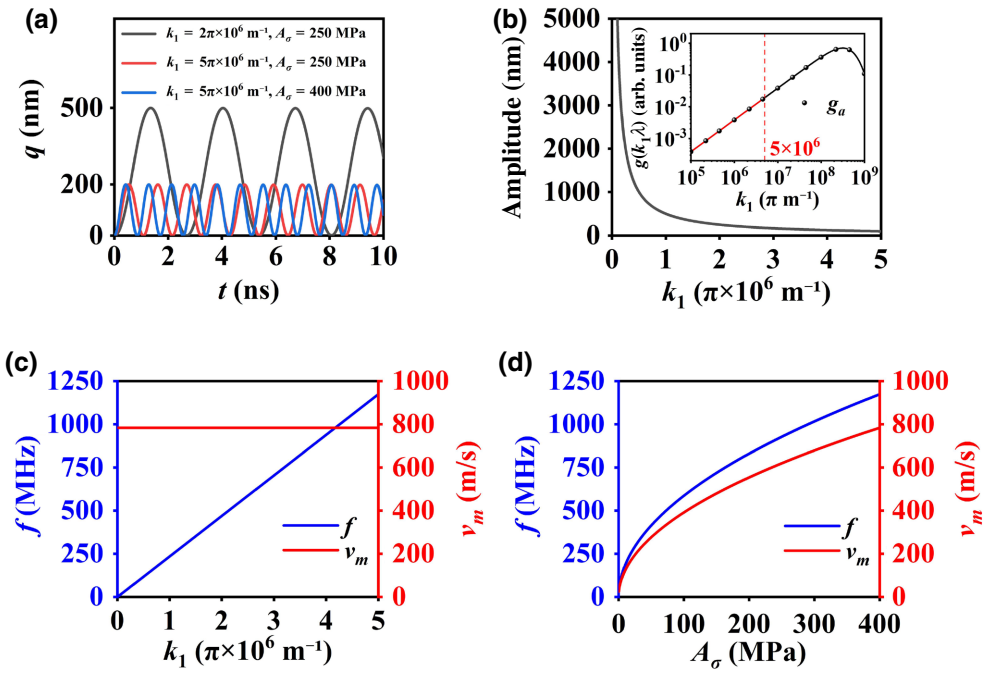

FIG. 2. (a) Representative oscillation of an AFM DW at different k_1 and A_σ. (b) Amplitude for the oscillation of an AFM DW as a function of k_1 from 0 to $5\pi \times 10^6$ m^{-1} [inset shows the factor g as a function of k_1. The solid line and dots are the numerical and analytical expression of the factor g($k_1\lambda$), respectively]. (c) Characteristic frequency (f) and the maximum velocity (v_m) for the oscillation of an AFM DW as a function of k_1 from 0 to $5\pi \times 10^6$ m^{-1}. (d) f and v_m as a function of A_σ [A_σ is 400 MPa in Figs. 2(b) and 2(c); k_1 is $5\pi \times 10^6$ m^{-1} in Fig. 2(d)].

Here, $\beta = (\pi/2) - qk_1$, and $\tilde{g} = (3J\lambda\gamma^2/2\mu_0^2)\lambda_s A_\sigma g(k_1\lambda)$. Equation (9) indicates the DW oscillation at a frequency f [23]:

$$f = \frac{\sqrt{6J\lambda\gamma^2\lambda_s A_\sigma k_1 g(k_1\lambda)}}{8\mu_0 \mathbf{K}\left(\frac{\sqrt{2}}{2}\right)}. \tag{10}$$

Here $\mathbf{K}(\sqrt{2}/2)$ is the first kind of complete elliptic integral:

$$\mathbf{K}\left(\frac{\sqrt{2}}{2}\right) = \int_0^{\pi/2} \frac{1}{\sqrt{1-\left(\frac{\sqrt{2}}{2}\right)^2 \sin^2(\theta)}} d\theta.$$

Since Eq. (9) is identical to an equation for the oscillation of a pendulum without damping, we can derive the maximum velocity (v_m) at the equilibrium position based on the conservation of mechanical energy: $(1/2)\tilde{m}v_m^2 = \tilde{m}\tilde{g}(1/k_1)$ with$\tilde{m}$, $\tilde{g}$, and $1/k_1$ representing mass, acceleration, and pendulum length, respectively. The v_m reflects the upper limit of DW velocity, and it is expressed as

$$v_m = \sqrt{\frac{2\tilde{g}}{k_1}} = \frac{\gamma}{\mu_0}\sqrt{\frac{3J\lambda\lambda_s A_\sigma g(k_1\lambda)}{k_1}}. \tag{11}$$

III. RESULTS AND DISCUSSION

The parameters of an AFM insulator NiO are used in the calculation [17]: K_0, A, M_s, d, λ_s, μ_0, and γ are 3.32×10^5 J/m^3, 5×10^{-13} J/m, 4.25×10^5 A/m, 4.2×10^{-10} m, 1.4×10^{-4}, $4\pi \times 10^{-7}$ N/A^2, and 2.21×10^5 m/(A s), respectively. The damping parameter α is smaller than 0.001 [24]. A_σ is 400 MPa or lower. Correspondingly, K_σ is at the magnitude of 10^4 J/m^3 or smaller, which is at least one order of magnitude smaller than K_0. Consequently, we can safely neglect the variation of λ with K in theory [17].

The oscillation of an AFM DW is also simulated based on a homemade code for solving the LLG equation of the magnetization in two sublattices of an AFM medium (see Fig. S1 within the Supplemental Material for more details [19]). The simulation is based on a discrete 1D chain model with the cell size being the same to the lattice constant (0.42 nm). The track dimension is 1050 nm (length) × 0.42 nm (width) × 0.42 nm (thickness).

As indicated in Eqs. (10) and (11), the DW oscillation is strictly relevant to the physical parameters including A_σ, k_1, and λ. Here λ and k_1 are the DW width and the reciprocal of spatial period of stress, respectively. Based on the resolution of current ultraviolet lithography technique, the smallest spatial period is hundreds of nanometers. Consequently, k_1 is at the magnitude of 10^7 m^{-1} or smaller. Here, we consider k_1 between 0 and $5\pi \times 10^6$ m^{-1} [inset of Fig. 2(b)].

As shown in Fig. 2, the changing of k_1 manipulates both characteristic frequency and amplitude [Figs. 2(a) and 2(c)], while A_σ only affects the frequency [Fig. 2(a)]. This is similar to a classical pendulum without damping. When k_1 is between 0 and $5\pi \times 10^6$ m^{-1}, the amplitude of DW oscillation is at the magnitude of hundreds of nanometers or larger [Fig. 2(b)]. On the other hand, the variation of k_1 in the range between 0 and $5\pi \times 10^6$ m^{-1} makes a negligible impact on v_m, which is around 800 m/s [Fig. 2(c)]. The v_m and characteristic frequency of an oscillating AFM DW (f) are also proportional to the square root of A_σ [Fig. 2(d)]. It is noteworthy that f is mostly at the magnitude of MHz [Figs. 2(c) and 2(d)], which is much lower than the characteristic frequency (THz or near THz) for the magnetization precession in an antiferromagnet driven by an ultrafast laser or voltage-induced spatiotemporal stress [5].

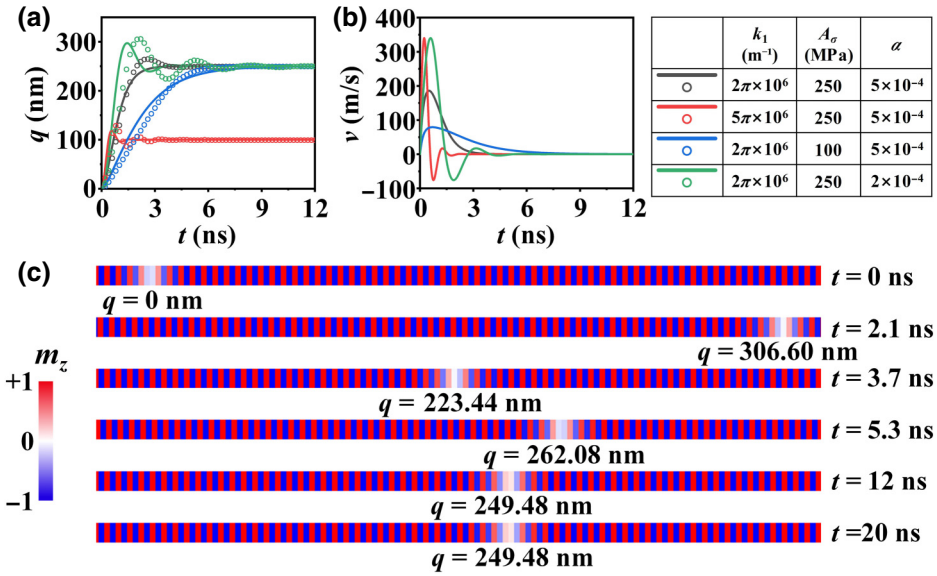

	k_1 (m^{-1})	A_σ (MPa)	α
○	$2\pi\times10^6$	250	5×10^{-4}
○	$5\pi\times10^6$	250	5×10^{-4}
○	$2\pi\times10^6$	100	5×10^{-4}
○	$2\pi\times10^6$	250	2×10^{-4}

FIG. 3. (a) Central position and (b) instantaneous DW velocity as a function of time at different physical parameters [the solid lines depict the numerical solutions of Eq. (8), and the dotted lines are the simulated results. The parameters for the simulation are listed in the table]. (c) Snapshot of simulated DW oscillation at different times for $k_1 = 5\pi \times 10^6$ m^{-1}, $A_\sigma = 250$ MPa, and $\alpha = 2 \times 10^{-4}$.

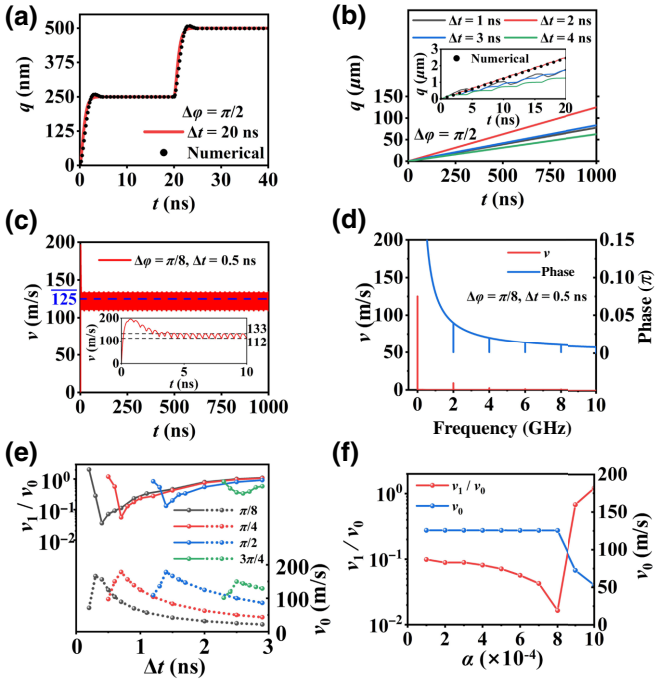

FIG. 4. (a) Temporal central position (q) for the DW motion driven by a pulsed stress wave with a phase shift of $\pi/2$ at $\Delta t = 20$ ns. (b) Temporal q for the DW motion driven by a pulsed stress wave with a phase shift of $\pi/2$ at different Δt (inset: the magnified $q \sim t$ curves in the first 20 ns). (c) Temporal AFM DW velocity for shifting the phase by $\pi/8$ at $\Delta t = 0.5$ ns (inset: magnified temporal AFM DW velocity in the first 10 ns). (d) Spectrum of phase and DW velocity of (c) using the FFT. (e) Velocity at zero frequency (v_0) and the ratio of velocity at the fundamental frequency (v_1) to v_0 as a function of Δt for different phase shifts; (f) v_0 and v_1/v_0 as a function of damping coefficient.

According to Eq. (10), even though strong AFM exchange coupling indeed contributes to the frequency of DW oscillation, the $g(k_1\lambda)$ factor seems more critical to the frequency of DW oscillation. This $g(k_1\lambda)$ is quite sensitive to the changing of k_1, and it significantly decreases by several magnitudes with the reducing of k_1 between 0 and $5\pi \times 10^6$ m^{-1} [inset of Fig. 2(b)]. Such a small k_1 corresponds to a spatial period that is much longer than DW width. Therefore, it is concluded that the slow DW oscillation is relevant to the size mismatch between the spatial period of stress and DW width.

The v_m in Fig. 2 indicates the upper limit of DW velocity with an idealistic zero damping coefficient. In real AFM medium, the influence of damping on the DW motion also needs to be taken into account. The equation containing the damping term [Eq. (8)] is numerically solved using the fourth-order Runge-Kutta algorithm with a time step of 10 ps, and the results are exhibited using the solid lines in Fig. 3(a). Because of damping, the DW fails to keep oscillating for a long time. Instead, it relaxes towards a stable equilibrium position that is hundreds of nanometers away from the origin of the coordinate system within 10 ns (Fig. 3). Increasing k_1 raises the frequency of DW oscillation and shifts the equilibrium position to be closer to the origin. Manipulation of A_σ changes the amplitude of DW oscillation, but influences neither relaxation time nor equilibrium position. In contrast, the enhancement of damping reduces the amplitude and accelerates the relaxation of the damped DW oscillation. The instantaneous DW velocity is derived by differentiating q with respect to t of the $q \sim t$ curves [Fig. 3(b)]. The velocity is smaller than v_m in Fig. 2. Nevertheless, a maximum DW velocity can still reach 350 m/s at a high k_1 or a lower damping coefficient.

The damped oscillation of an AFM DW is also simulated using the homemade code as illustrated by the circles in Fig. 3(a) (the movie is shown in Video S1 in the Supplemental Material [19]). Overall, the simulated DW oscillation is close to the numerical solution of Eq. (8). However, at very weak damping, the simulated oscillation seems slower than that from solving Eq. (8). This difference may come from the *linear* approximation in CCM for deriving Eq. (8). On the other hand, the variation of DW width is neglected in CCM but is included in the simulation. The changing of DW width in the simulation can be different from that determined from the continuous CCM. For example, the variation of anisotropy constant between 2.48×10^5 J/m^3 and 4.16×10^5 J/m^3 ($A_\sigma = 400$ MPa) leads to the theoretical changing of DW width between 1.10 and 1.42 nm. This is even shorter than a cell in the simulation. The contradiction between CCM and simulation deserves further investigation [25].

Figure 3 exhibits stress-induced DW oscillation with a decaying amplitude towards an equilibrium position. In real application, continuous DW motion at a stable velocity seems more relevant. This demands the shift of equilibrium position at a speed matching the DW velocity under spatiotemporal stress. A typical example of spatiotemporal stress is surface acoustic wave (SAW). However, our calculation indicates that it is still quite challenging to trigger the AFM DW motion at a controllable speed by SAW (Fig. S3 within the Supplemental Material [19]). Nevertheless, steady DW motion is still possible under a sinusoidal stress function with an abrupt phase shift at a fixed period (Fig. 4).

At first, as an extreme case, we consider the phase shift of $\pi/2$ after the DW halts moving at its equilibrium position under the first triggering. The abrupt change of phase φ by $\pi/2$ removes the equilibrium position. As a result, the DW moves again towards the next equilibrium position [Fig. 4(a)]. This is the principle for observing DW motion by a magneto-optical Kerr effect (MOKE) microscope.

On the other hand, when the phase is shifted before the DW relaxes to the equilibrium position, the DW can move continuously. As representative examples, we consider a

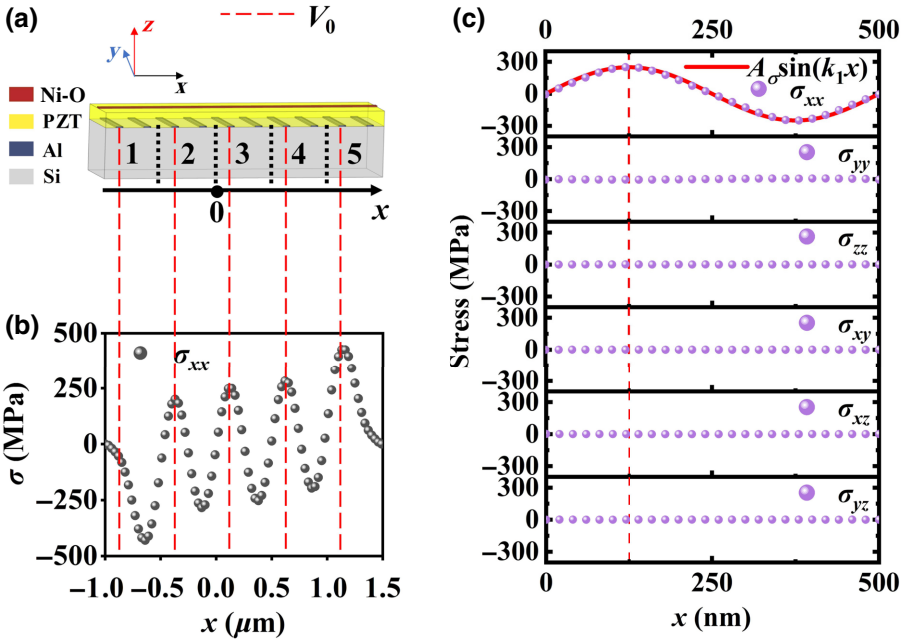

FIG. 5. (a) Schematic of the structure of the device for AFM DW motion induced by position-dependent stress as a sinusoidal function in a spatial coordinate. (b) Simulated xx component of the stress (σ_{xx}) as a function of the coordinate x in the length range shown in (a). (c) Simulated stress components (σ_{xx}, σ_{yy}, σ_{zz}, σ_{xy}, σ_{xz}, and σ_{yz}) as a function of x from 0 to 500 nm (the dotted lines) and the fitted σ_{xx} as a sinusoidal function of x (the red solid line) (the red dash lines indicate where the voltage is applied).

phase shift of $\pi/2$ at Δt of 1, 2, 3, and 4 ns after the initial triggering [Fig. 4(b)]. They are all much shorter than the relaxation time. Consequently, the q-t curves in Fig. 4(b) indicate sustainable DW motion within 1000 ns, and the average DW velocity becomes maximum (around 130 m/s) when $\Delta t = 2$ ns. To exhibit the DW motion in a time range that is comparable to the pulse period, we magnify the q-t curves in the initial 20 ns [inset of Fig. 4(b)]. In this time range, the DW motion is similar to that in the long stage of 1000 ns. On the other hand, the result of simulation [the black dotted line in the inset of Fig. 4(b)] is very close to that of the numerical solution of Eq. (8) (the movie is shown in Video S2 within the Supplemental Material [19]).

To exhibit the characteristics of DW motion more clearly, we derive instantaneous DW velocity by differentiating q with respect to t. As a representative case for $\Delta\varphi = \pi/8$ and $\Delta t = 0.5$ ns [Fig. 4(c)], the DW velocity can be controlled around 125 m/s after short initial relaxation. This means that uniform motion and small oscillation compose the DW motion. The time-dependent DW velocity and phase are transformed into frequency domain using fast Fourier transformation (FFT) analysis. (The frequency, time interval, and point number for the sampling are 100 GHz, 0.01 ns, and 10^5, respectively.) In the frequency domain, the amplitude of phase at zero frequency approaches infinite and it drops to zero at a series of frequencies ($f_n = 2n$ GHz, $n = 1, 2, 3$, etc.) (this is explained in detail in Fig. S4 within the Supplemental Material [19]). Correspondingly, the amplitude of DW velocity consists of a large value at zero frequency (v_0) for the average velocity and a series of small amplitudes at f_n (v_n, $n = 1, 2, 3$, etc.). Therefore, under the pulsed phase, the DW motion is composed by uniform motion and small oscillation.

In application, one may expect the uniform motion dominates over oscillation. Therefore, we collect v_0 and v_1/v_0 at different conditions [v_n ($n > 1$) is negligible] [Figs. 4(e) and 4(f)]. Both v_0 and v_1/v_0 nonmonotonously change with Δt. When Δt is very short, the DW cannot accelerate to a high speed. After the relaxation for a long Δt, the DW slows down due to damping [Fig. 4(f)]. On the other hand, the maximum v_0 is accompanied with the minimum v_1/v_0 that is smaller than 0.1 [Fig. 4(e)], showing the dominant uniform motion over oscillation.

Finally, we simulate the position-dependent stress that triggers the motion of an AFM DW using the software COMSOL Multiphysics (Figs. 5 and 6). The simulated device comprises NiO nanowire, lead zirconate titanate (PZT) layer, Al electrode array, and Si substrate from top to bottom [Fig. 5(a)]. The distance between neighboring Al electrodes is 250 nm. The result of simulation shows that the x-dependent xx component of the stress (σ_{xx}) satisfies a sinusoidal function when the position is more than 500 nm away from the edge [Figs. 5(b) and 5(c)]. On the other hand, because of the geometry of the long-stripe nanowire, σ_{xx} is clearly dominant over all the other components [Fig. 5(c)]. This confirms the validity for considering σ_{xx} in the theoretical calculation above.

In experiments, the phase of sinusoidal stress function can be shifted through the circuit as shown in Fig. 6(a). In this circuit, the position-dependent stress is generated under a voltage pulse, and the phase of sinusoidal stress function can be shifted by the delayer connecting to the electrode. The temporal voltage pulse with $V_0 = 5.7$ V [Fig. 6(b)] triggers the stress as a sinusoidal function in a spatial coordinate [Fig. 6(c)]. Here, the phase of sinusoidal stress function is shifted by $\pi/2$ at time Δt with

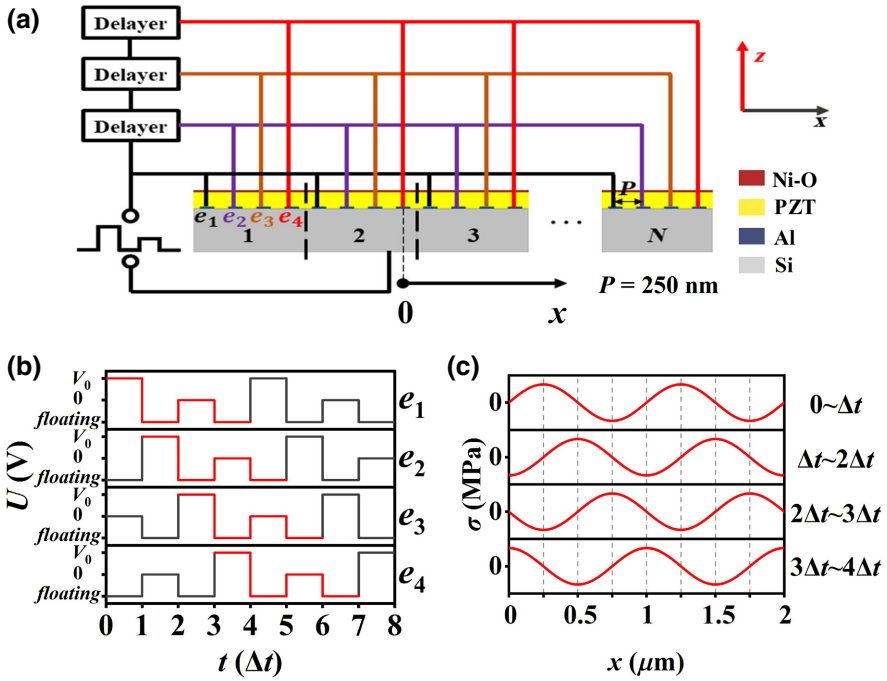

FIG. 6. (a) Structure of the circuit for generating position-dependent stress with switchable phase. (b) Time-dependent electrical potential on the e_1, e_2, e_3, and e_4 points shown in (a). (c) Simulated stress as a sinusoidal function of x due to the pulsed voltage in (b) with phase shift of $\pi/2$ at Δt with a period of $4\Delta t$.

a period of $4\Delta t$, which can induce continuous motion of an AFM DW. On the other hand, the relaxation time of voltage-induced variation of stress is at the magnitude of picoseconds, which is several magnitudes shorter than relaxation of AFM DW [5]. Therefore, its influence on DW dynamics can be safely neglected.

Finally, the dissipation of the system in Fig. 6 is estimated. Under the assumption for an idealistic insulating PZT substrate, the dissipation only comes from the magnetization precession with Gilbert damping. When the AFM DW moves at a velocity around 100 m/s, the emission of spin wave can be neglected, and the dissipation is approximated as $P_{\rm dis} = -2\mu_0 H_{\rm eff} M_s v d^2$ [25]. Since the DW velocity is $v = \gamma H_{\rm eff}\lambda/\alpha$ [26], the $P_{\rm dis}$ can be expressed as $P_{\rm dis} = (2\mu_0 M_s v^2 d^2 \alpha)/\gamma\lambda$. Assuming $v = 100$ m/s and $\alpha = 5 \times 10^{-4}$, the power of dissipation is around 3.5×10^{-15} W.

IV. SUMMARY

In summary, MHz oscillation and steady motion of an AFM DW driven by spatial-dependent stress are investigated in theory. Under an experimentally reasonable sinusoidal stress function, the DW oscillates around an equilibrium position at the frequency of MHz. This low frequency of DW oscillation is because of the size mismatch between the spatial period of stress and DW width. When the phase of stress is shifted during the relaxation of DW, the DW can continuously move at a controllable velocity that is higher than 100 m/s. This contributes to the manipulation of DW motion at a stable velocity in a single AFM insulator and paves the way to develop AFM spintronics devices with an ultralow dissipation. On the other hand, similar interesting phenomena may also be observed for different AFM textures, such as AFM skyrmion. This deserves further investigation.

ACKNOWLEDGMENT

The authors acknowledge financial support from the National Natural Science Foundation of China (Grants No. 51971098, No. 11874169, No. 91963207), Science and Technology Department of Hubei Province (Grant No. 2019CFB435), and National Undergraduate Training Projects for Innovation and Entrepreneurship (Grant No. 5003182007). We also acknowledge the valuable suggestion provided by Prof. Weiwei Lin of the School of Physics, Southeast University in China.

[1] V. Baltz, A. Manchon, M. Tsoi, T. Moriyama, T. Ono, and Y. Tserkovnyak, Antiferromagnetic spintronics, Rev. Mod. Phys. **90**, 015005 (2018).
[2] T. Jungwirth, X. Marti, P. Wadley, and J. Wunderlich, Antiferromagnetic spintronics, Nat. Nanotechnol. **11**, 231 (2016).
[3] B. A. Ivanov, Spin dynamics of antiferromagnets under action of femtosecond laser pulses (review article), Low Temp. Phys. **40**, 91 (2014).
[4] T. Kampfrath, A. Sell, G. Klatt, A. Pashkin, S. Mährlein, T. Dekorsy, M. Wolf, M. Fiebig, A. Leitenstorfer, and R. Huber, Coherent terahertz control of antiferromagnetic spin wave, Nat. Photonics **5**, 31 (2011).
[5] A. Barra, J. Domann, K. W. Kim, and G. Carman, Voltage Control of Antiferromagnetic Phases at Near-Terahertz Frequencies, Phys. Rev. Appl. **9**, 034017 (2018).

[6] E. A. Mashkovich, K. A. Grishunin, R. V. Mikhaylovskiy, A. K. Zvezdin, R. V. Pisarev, M. B. Strugatsky, P. C. M. Christianen, Th. Rasing, and A. V. Kimel, Terahertz Optomagnetism: Nonlinear THz Excitation of GHz Spin Waves in Antiferromagnetic FeBO3, Phys. Rev. Lett. **123**, 157202 (2019).

[7] R. Wieser, E. Y. Vedmedenko, and R. Wiesendanger, Indirect Control of Antiferromagnetic Domain Walls with Spin Current, Phys. Rev. Lett. **106**, 067204 (2011).

[8] C. D. Jin, C. K. Song, J. B. Wang, and Q. F. Liu, Dynamics of antiferromagnetic skyrmion driven by the spin Hall effect, Appl. Phys. Lett. **109**, 182404 (2016).

[9] X. C. Zhang, Y. Zhou, and M. Ezawa, Antiferromagnetic skyrmion: Stability, creation and manipulation, Sci. Rep. **6**, 24795 (2016).

[10] S. Selzer, U. Atxitia, U. Ritzmann, D. Hinzke, and U. Nowak, Inertia-Free Thermally Driven Domain-Wall Motion in Antiferromagnets, Phys. Rev. Lett. **117**, 107201 (2016).

[11] L. C. Shen, J. Xia, G. P. Zhao, X. C. Zhang, M. Ezawa, O. A. Tretiakov, X. X. Liu, and Y. Zhou, Dynamics of the antiferromagnetic skyrmion induced by a magnetic anisotropy gradient, Phys. Rev. B **98**, 134448 (2018).

[12] T. Shiino, S. H. Oh, P. M. Haney, S. W. Lee, G. Go, B. G. Park, and K. J. Lee, Antiferromagnetic Domain Wall Motion Driven by Spin-Orbit Torques, Phys. Rev. Lett. **117**, 087203 (2016).

[13] O. Gomonay, T. Jungwirth, and J. Sinova, High Antiferromagnetic Domain Wall Velocity Induced by Néel Spin-Orbit Torques, Phys. Rev. Lett. **117**, 017202 (2016).

[14] K. M. D. Hals, Y. Tserkovnyak, and A. Brataas, Phenomenology of Current-Induced Dynamics in Antiferromagnets, Phys. Rev. Lett. **106**, 107206 (2011).

[15] E. G. Tveten, A. Qaiumzadeh, and A. Brataas, Antiferromagnetic Domain Wall Motion Induced by Spin Waves, Phys. Rev. Lett. **112**, 147204 (2014).

[16] O. Gomonay, V. Baltz, A. Brataas, and Y. Tserkovnyak, Antiferromagnetic spin textures and dynamics, Nat. Phys. **14**, 213 (2018).

[17] F. Chen, Z. D. Zhang, W. Luo, X. F. Yang, L. You, and Y. Zhang, Voltage-induced inertial domain wall motion in an antiferromagnetic nanowire, J. Magn. Magn. Mater. **511**, 166995 (2020).

[18] S. Sugimoto, Y. Nakatani, Y. Yamane, M. Ikhlas, K. Kondou, M. Kimata, T. Tomita, S. Nakatsuji, and Y. Otani, Electrical nucleation, displacement, and detection of antiferromagnetic domain walls in the chiral antiferromagnet Mn_3Sn, Communications Physics **3**, 1 (2020).

[19] See Supplemental Material at http://link.aps.org/supplemental/10.1103/PhysRevApplied.15.014030 for the model and method of the numerical simulation (Fig. S1), movies of the simulated motion of an AFM DW (Videos S1 and S2), the numerical investigation about the oscillation of an AFM DW driven by surface acoustic wave (Fig. S3), and the explanation about the abrupt dropping of the amplitude of phase at the characteristic frequency as shown in Fig. 4(d) (Fig. S4).

[20] E. G. Tveten, A. Qaiumzadeh, O. A. Tretiakov, and A. Brataas, Staggered Dynamics in Antiferromagnets by Collective Coordinates, Phys. Rev. Lett. **110**, 127208 (2013).

[21] J. Dean, M. T. Bryan, J. D. Cooper, A. Virbule, J. E. Cunningham, and T. J. Hayward, A sound idea: Manipulating domain walls in magnetic nanowires using surface acoustic waves, Appl. Phys. Lett. **107**, 142405 (2015).

[22] M. T. Bryan, J. Dean, and D. A. Allwood, Dynamics of stress-induced domain wall motion, Phys. Rev. B **85**, 144411 (2012).

[23] R. R. Parwani, An approximate expression for the large angle period of a simple pendulum, Eur. J. Phys. **25**, 37 (2004).

[24] T. Moriyama, K. Hayashi, K. Yamada, M. Shima, Y. Ohya, and T. Ono, Intrinsic and extrinsic antiferromagnetic damping in NiO, Phys. Rev. Materials **3**, 051402(R) (2019).

[25] H. Yang, H. Y. Yang, M. Yan, H. W. Zhang, and P. Yan, Atomic antiferromagnetic domain wall propagation beyond the relativistic limit, Phys. Rev. B **100**, 024407 (2019).

Correction notice: The "Corresponding author" identifier was removed from the byline footnotes for the third and tenth authors during the proof cycle and has been restored. The order of the byline footnotes has also been fixed.